eMagRes
MRI | NMR

Pulse Sequences for Hyperpolarized MRS

Jeremy W. Gordon & Peder E.Z. Larson

University of California – San Francisco, San Francisco, CA, USA

Hyperpolarization offers substantial gains in sensitivity for magnetic resonance (MR) spectroscopy (MRS) and imaging (MRI), which are particularly beneficial for providing novel functional information not accessible to conventional MRS and MRI. However, hyperpolarized MR requires tailored pulse sequences because of its unique magnetization behavior, including its decay back to thermal equilibrium, spin exchange, and metabolic conversion of the hyperpolarized magnetization. In addition, rapid delivery of the hyperpolarized media from the polarizer to the subject is key to success. This article begins by describing the unique behavior of hyperpolarized agents and the problems associated with their delivery, focusing on ^{13}C-labeled pyruvate. Efficient RF and acquisition strategies that include variable flip angles, spectral-spatial RF pulses that address problems with chemical shift displacement artifacts, hyperpolarized slice profile distortions, and the effects of magnetic field inhomogeneity are presented. Acquisition strategies covered include MR spectroscopic imaging with phase encoding and time-dependent readout gradient trajectories, model-based methods, metabolite-specific imaging, steady-state free-precession, and ultrafast two-dimensional NMR. The integration of compressed sensing and parallel imaging into hyperpolarized MR for acceleration is also examined.

Keywords: hyperpolarized pulse sequences, metabolic imaging, molecular imaging, variable flip angles, spectral-spatial RF pulses, rapid spectroscopic imaging, metabolite-specific imaging, ultrafast 2-D NMR

How to cite this article:
eMagRes, 2016, Vol 5: 1229 – 1246. DOI 10.1002/9780470034590.emrstm1451

Introduction

Magnetic resonance (MR) is typically considered an insensitive imaging technique; and while magnetic resonance imaging (MRI) is used routinely to provide structural imaging with exquisite soft-tissue contrast, the poor sensitivity limits the utility of magnetic resonance spectroscopy (MRS) and non-proton MRI. MRS of both proton (^{1}H) and non-proton nuclei have the capability of providing valuable and unique functional information that is not provided by conventional proton MRI methods; thus, methods that improve its sensitivity are of high interest.

Hyperpolarization techniques can offer substantial improvements in sensitivity by increasing the spin polarization orders of magnitude above thermal polarization levels, opening up new applications for MRS. Using hyperpolarization efficiently for MRS requires tailored pulse sequences that address several unique challenges, including its decay back to thermal equilibrium, spin exchange and metabolic conversion of the hyperpolarized (HP) magnetization, and the requisite high-speed delivery of HP media from the polarizer to the subject. This article describes the unique challenges of HP pulse sequence design, and state-of-the-art radio frequency (RF) pulse and acquisition strategies that address these challenges. Several other relevant articles in this book include ***Hyperpolarization Methods for MRS*** on the physics and apparatus for HP, ***Hyperpolarized Carbon-13 MRI and MRS Studies*** concerning applications of HP technology, and ***Integration of ^{13}C Isotopomer Methods and Hyperpolarization Provides a Comprehensive Picture of Metabolism***, which investigates metabolic pathways.

Evolution of Hyperpolarized Agents

Hyperpolarized Signal Decay

The end result of hyperpolarization via any technique is a nuclear polarization above that achieved via Boltzmann thermal equilibrium alone. For example, with dissolution dynamic nuclear polarization (DNP), many carbon-13 (^{13}C)-labeled molecules can be polarized to levels $\geq$ 20%, which is over 10 000-fold larger than their thermal polarizations at clinical magnetic field strengths of $B_0 = 1.5$ or 3 T. This enables imaging of ^{13}C-labeled molecules on short timescales, which would normally be impossible. However, because the polarization is produced exogenously (i.e., in a hyperpolarizer), the longitudinal magnetization $M_z(t)$ decays to thermal equilibrium over time (t) rather than recovering to its initial HP state:

$$M_z(t) = M_0 + (M_{z,\mathrm{HP}} - M_0)\exp\left(-\frac{t}{T_1}\right) \cong M_{z,\mathrm{HP}}\exp\left(-\frac{t}{T_1}\right) \quad (1)$$

Here, $M_{z,\mathrm{HP}}$ is the initial HP magnetization, M_0 is the thermal equilibrium magnetization, and T_1 is the longitudinal relaxation time of the nuclei. The approximation is valid if the HP magnetization is much larger than the thermal equilibrium magnetization. We will typically assume this is the case, and that once the nuclei have decayed to their thermal polarization they no longer provide sufficient signal for rapid imaging or

MRS techniques. As a consequence, there is a short timeframe in which to acquire data. For example, the T_1 values for typical HP ^{13}C substrates are on the order of 60s in solution and decrease to 30s in vivo.[1]

Implicit within this, however, is that each RF excitation pulse consumes some of the finite HP magnetization. In the case where n RF excitations of the same flip angle θ are applied, M_z and the transverse magnetization, (M_{xy}), at time t are given by[2]

$$M_z(t) = M_{z,HP} \exp\left(-\frac{t}{T_1}\right) \cos^{n-1}\theta \qquad (2)$$

$$M_{xy}(t) = M_{z,HP} \exp\left(-\frac{t}{T_1}\right) \cos^{n-1}\theta \sin\theta \qquad (3)$$

Thus, T_1 and data acquisition both result in unrecoverable signal decay of the HP magnetization. For rapid (sequence repetition period, $TR \ll T_1$) acquisitions in the absence of metabolism, the exponential term can be ignored and the magnetization is solely a function of the RF excitation. This means that signal averaging or experiments that require $\theta = 90°$ excitations are generally incompatible with HP experiments.

Delivery, Uptake, and Metabolism

Unlike conventional MRI, where the polarization is derived from the temperature of the subject or sample and B_0, hyperpolarization provides an exogenous increase in magnetization that is independent of both factors. While this enables near real-time metabolic imaging, it also imposes numerous experimental limitations due to the fact that the HP substrate must have a rapid delivery, uptake, and metabolic conversion prior to the decay of the transient hyperpolarization. There are also limitations on the molecules that are suitable for HP MRS studies. They must fulfill chemical and physical requirements to achieve high polarizations, be polarizable and nontoxic at relatively high concentrations (millimolar for in vivo studies), and undergo rapid transport and in vivo reaction kinetics of interest on the timescale of T_1 (see ***Hyperpolarized Carbon-13 MRI and MRS Studies***).[3]

This article primarily considers and exemplifies the case of [1-^{13}C]pyruvate, HP via dissolution DNP. Considering the above criteria, pyruvate is perhaps the ideal compound for hyperpolarization via DNP. The pure acid is a high-molarity liquid (14.2 M) at room temperature and forms a glassy matrix in the presence of a trityl radical, facilitating high polarization levels (>50% at 5 T and 0.8 K). Both the C1 and C2 carbon positions are quaternary, resulting in relatively long T_1 times (50–60 s[4]) in solution. In addition, sitting at the nexus of aerobic and anaerobic metabolism, pyruvate is rapidly transported into the cell via monocarboxylate transporters[5] and is enzymatically converted into its product metabolites, including lactate, alanine, and bicarbonate, on the imaging timescale. Pyruvate and its downstream metabolites resonate at different frequencies, owing to the local chemical environment and the degree to which they are shielded from the main applied magnetic field by their valence shell electrons. This enables both reactants and products to be unambiguously differentiated by MRS techniques, from which measures of the metabolic reaction kinetics can be derived by monitoring their time course. For these reasons, [1-^{13}C]pyruvate is the most widely used HP MRS agent, and has been applied in human studies.[6]

The goal of HP MRS pulse sequences then is to capture the conversion from substrate, pyruvate, to product, lactate, alanine, and/or bicarbonate, both efficiently and quantitatively (Figure 1). This requires that multiple compounds at different resonance frequencies are excited and resolved, whether by spectroscopic or direct imaging methods, as described later. In order to describe the metabolism dynamics, we use an exchange model commonly applied to the in vivo kinetics of HP pyruvate and its conversion to lactate. (A similar model can be applied to many other compounds: see ***Integration of ^{13}C Isotopomer Methods and Hyperpolarization Provides a Comprehensive Picture of Metabolism***.) The dynamic pyruvate and lactate signals are commonly fitted to a two-site exchange model[7]:

$$P \underset{k_L}{\overset{k_P}{\rightleftarrows}} L$$

$$\frac{dL_z}{dt} = -\rho_L(L_z - L_\infty) + k_P P_z - k_L L_z \qquad (4)$$

$$\frac{dP_z}{dt} = -\rho_P(P_z - P_\infty) + k_L L_z - k_P P_z$$

In this nomenclature, L_z and P_z denote the lactate and pyruvate magnetization, ρ_L and ρ_P are the lactate and pyruvate spin–lattice relaxation rates ($1/T_1$), and k_p and k_L are the apparent forward and reverse rate constants (per second) for the reaction. More sophisticated models that include attempts to account for the rate of inflow,[8] diffusion across the blood-tissue (e.g. brain) barrier[9], and variations in the arterial input function can also be applied.[10]

In general, two experimental strategies have been applied for measuring metabolism using HP agents: (i) single time-point methods, where ratios of compounds are used as a measure of conversion, and (ii) dynamic methods, which seek to fit a kinetic model, such as the two-site model above. While a single time-point dataset and analysis of, for example, the lactate/pyruvate ratio, is sufficient to detect metabolic changes, this technique is sensitive to and does not account for confounding factors such as differences in perfusion, injection volume, or the time between injection and image acquisition, to name only a few. Dynamic methods are more robust to these confounding factors, but require more rapid acquisition strategies and also that the HP magnetization be distributed across multiple datasets. The RF pulse strategies described in the section titled 'RF Pulse Strategies' address how to utilize the magnetization for single time-point or for dynamic experiments. The majority of the acquisition methods described thereafter can be applied to both of these experimental strategies except where noted otherwise.

RF Pulse Strategies

Great care must be taken when choosing RF pulse strategies in HP MRS because each pulse results in depletion of the nonrenewable HP state. The RF pulse strategies must efficiently use

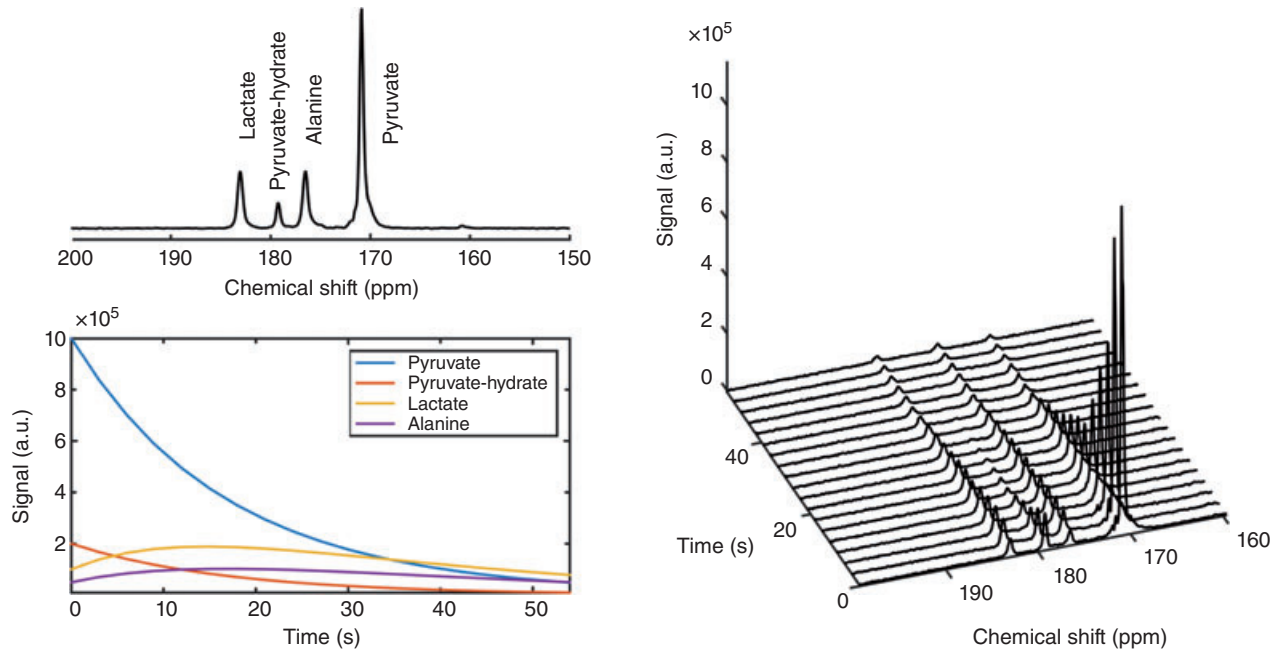

Figure 1. Dynamics and chemical shift of metabolites following injection of [1-^{13}C]pyruvate. A typical dynamic slab spectrum shows strong pyruvate signal (171 ppm) along with conversion to lactate (183 ppm) and alanine (176 ppm) in the timescale of the hyperpolarized experiment (top left and at right). Pyruvate-hydrate (179 ppm) is a nonmetabolized compound that is in slow equilibrium with pyruvate, and its concentration is a function of pH. To accurately capture and quantify the kinetics, data are acquired at multiple time points along the dynamic time curve (bottom left)

the HP magnetization considering all of the RF pulses being applied in toto. The spectral (frequency) profile of the RF pulses must also be considered because of the multiple compounds and resonance frequencies present in typical HP experiments.

In general, a larger flip angle (θ) leads to a more rapid decay of M_z but initially provides a larger M_{xy}. In contrast, a small flip angle preserves M_z while providing a small but relatively constant M_{xy}. In k-space, this signal modulation results in filtering that will affect image quality (Figure 2). For example, application of a sequential phase-encoding scheme that starts from a corner of k-space with a constant flip angle will act as a high-pass filter, resulting in undesired emphasis on high-spatial frequencies, which are sampled first, at the expense of signal-to-noise ratio (SNR). A centric-view ordering, starting from the center of k-space, will alternatively act as a low-pass filter, resulting in a blurred image but with improved SNR. If the B_1 is properly calibrated, a variable flip angle (VFA) approach can provide constant magnetization at each TR by increasing the flip angle to compensate for the decline in magnetization after each pulse. This approach maximizes SNR while minimizing artifacts and makes the most efficient use of the HP signal. The details are discussed next.

Variable Flip Angles

When multiple RF pulses are required, VFA strategies provide efficient and equalized usage of the HP magnetization. To compensate for the effect of the preceding RF pulse, but neglecting T_1 decay and metabolic conversion, a constant signal amplitude as well as optimal total SNR is achieved by using flip angles of

$$\theta_n = \tan^{-1}\left(\frac{1}{\sqrt{N-n}}\right) \quad (5)$$

for the nth RF pulse of a sequence using a total of N pulses.[2] We will call this the 'RF-compensated VFA' strategy. Interestingly, summing all the signals after each RF pulse yields a total signal proportional to M_0, regardless of N, assuming no decay or conversion. If T_1 decay cannot be neglected (i.e., NTR $\geq T_1$), then two different VFA strategies can be used to achieve either constant signals after each pulse, $\theta_{n,\text{flat}}$, or to maximize the summed signals from all pulses, $\theta_{n,\text{max}}$[2,11]:

$$\theta_{n,\text{flat}} = \cos^{-1}\sqrt{\frac{1-E_1^{2(N-n+1)}}{1-E_1^{2(N-n+1)}}} \quad (6)$$

$$\theta_{n,\text{max}} = \cos^{-1}\sqrt{\frac{E_1^2-E_1^{2(N-n+1)}}{1-E_1^{2(N-n+1)}}} \quad (7)$$

where $E_1 = \exp(-\text{TR}/T_1)$ accounts for the signal decay during each TR.

Metabolite-specific Flip Angles

Given the presence of multiple compounds, HP MRS strategies should always consider the frequency-selective properties of the RF pulses. Designing the frequency profile of RF pulses to specifically control the flip angles for different compounds can improve the speed and SNR of HP MRS experiments.

One way to improve the SNR in dynamic HP MRS experiments is to apply lower flip angles to the substrate as compared to the metabolic products. This is a so-called multiband

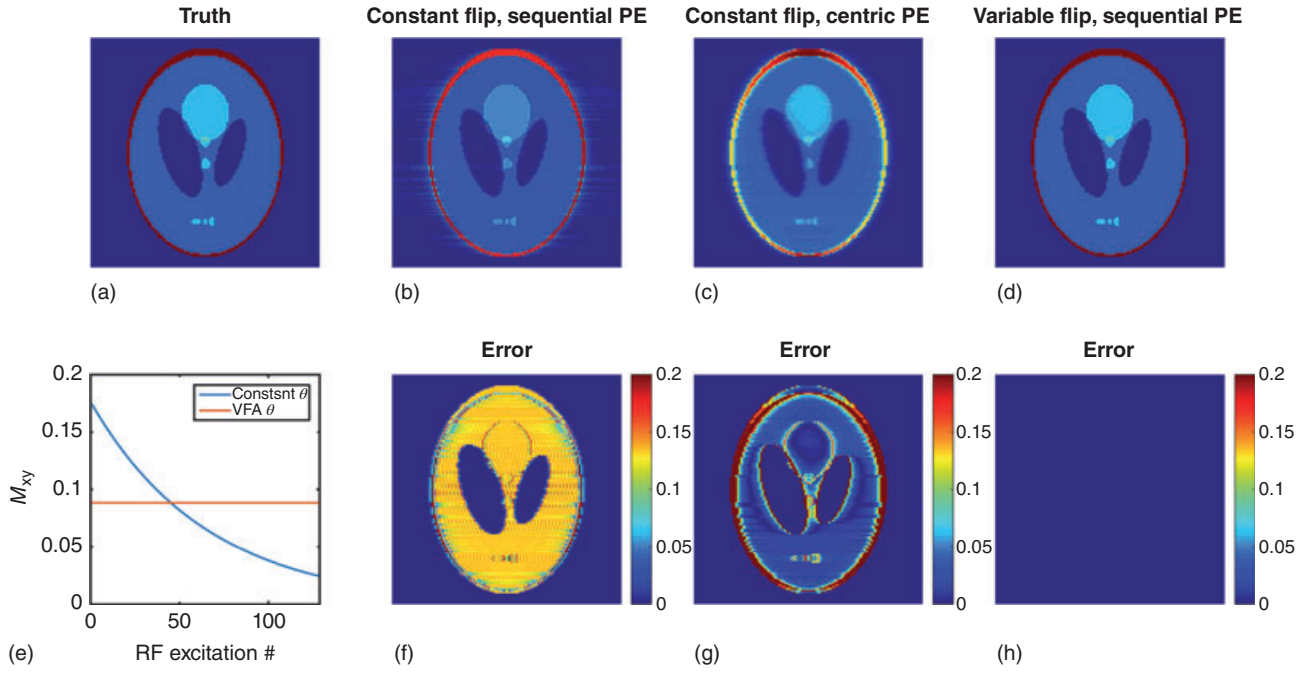

Figure 2. Compared to the ground truth (a), this can introduce spatial filtering effects, resulting in the effect of flip angle filtering on image quality in an HP experiment. Due to the nonequilibrium magnetization, each RF pulse consumes some of the nonrecoverable magnetization. Compared to the ground truth (a), this can introduce spatial filtering effects, resulting in an effective high-pass (b,f) or low-pass (c,g) filter for a constant flip angle, depending on the phase-encoding scheme. A variable flip angle approach increases the flip angle for each subsequent RF pulse, accounting for the reduced magnetization and resulting in a constant signal profile for all phase encodes (d,e,h)

approach.[12,13] Typically there is much more HP magnetization available for the substrate (e.g., pyruvate) as compared to the metabolic products (e.g., lactate, alanine). In this case, a lower flip angle can be applied to the substrate compared to a higher flip angle for the product(s). This results in reduced usage of the substrate's HP magnetization, allowing for continued conversion to the product(s) that will improve the SNR of subsequent dynamic datasets. When the flip angles are chosen properly, adequate SNR can be provided for all compounds of interest.

The multiband approach can also be combined with varying flip angles across time for more efficient magnetization usage (termed 'multiband VFA'). One simple method to choose these flip angles is the so-called T_1-effective approach, which uses equation (6) but substitutes an effective T_1 rate that includes metabolic conversion.[13] This is based on the observation that a substrate and product (e.g., pyruvate and lactate) in a two-site exchange model [equation (4)] with one-directional conversion have approximate relaxation rates of $R_{1P,\mathrm{eff}} = \frac{1}{T_{1P}} + K_{PL}$ which includes the speed up in the pyruvate rate due to its conversion to lactate; and $R_{1L,\mathrm{eff}} = \frac{1}{T_{1L}} - K_{PL}$ which includes the magnetization gained from conversion. This is analogous to the treatment used for rate measurements in magnetization transfer experiments (see ***Measuring Biochemical Reaction Rates In Vivo with Magnetization Transfer***). With this approach, the flip angles are defined the same as in equation (6), except that E_1 is replaced by $E_{1,\mathrm{eff}} = \exp(-\mathrm{TR}\cdot R_{1,\mathrm{eff}})$ using the apparent relaxation rates that are observed. This 'T_1-effective' approach results in an approximately flat signal response. The multiband VFAs can also be chosen for maximum summed product SNR by using equation (7) for the product flip angles with the estimated T_1.

Another metabolite-specific flip angle strategy for dynamic HP MRS is to use a saturation-recovery flip angle schedule, where the product is given a 90° flip angle for each dynamic dataset, while the substrate is excited by a small flip angle.[14] The advantage of this approach is that the amplitudes in each dynamic product dataset are simply determined by the metabolic conversion rate and the TR, which greatly simplifies the quantification of the metabolic kinetics.

Figure 3 demonstrates the flip angles and simulated signal resulting from various RF pulse strategies. The relative summed product SNRs in this simulation were 0.2591 (constant), 0.2922 (multiband), 0.3100 (RF-compensated VFA), 0.3304 (multiband VFA), and 0.1608 (saturation recovery), illustrating that the VFA approaches provide the largest summed SNRs. With any metabolite-selective flip angle approach, the varying flip angles between compounds must be accounted for in the image analysis.[15]

RF Pulse Design

Spectrally selective RF pulses for HP MRS can be designed using many methods, but we recommend the Shinnar–Le Roux (SLR) pulse design method for its accuracy and ease of use.[16] Spectral-spatial (SPSP) RF pulses are more challenging to design, but allow for slice or slab-selective acquisitions as well as frequency-specific flip angles.[17] There is a MATLAB (MathWorks, Inc., Natick MA, USA) SPSP RF pulse design

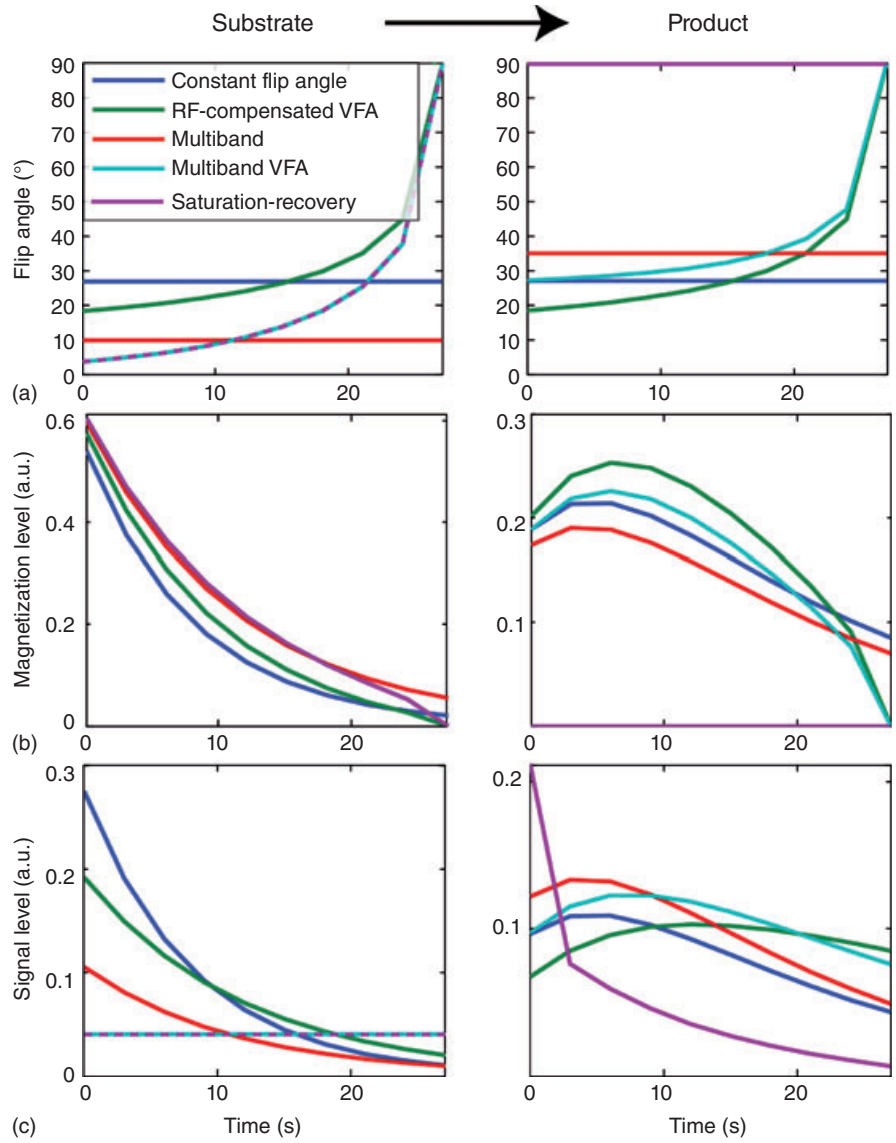

Figure 3. Flip angle schedules and simulated results from various RF pulse strategies, showing the substrate (e.g., pyruvate) and product (e.g., lactate) (a) flip angles, (b) simulated longitudinal magnetization, and (c) simulated transverse magnetization (i.e., signal). The simulations assumed an initial buildup of the product prior to acquisition; longitudinal relaxation times (T_1) of 30 s; a substrate-to-product conversion rate of $K_{12} = 0.05\ s^{-1}$ (with no product-to-substrate conversion); repetition time, TR = 3 s; and a total acquisition time of 30 s. In this simulation, the constant (27°; dark blue curve) and multiband (10°, 35°; red curves) flip angles were individually optimized for maximum summed product SNR. The multiband variable flip scheme (cyan curve) was also optimized for maximum summed product SNR using equation (7) for the product flip angles. The multiband VFA substrate scheme was also used for the saturation-recovery scheme (purple curves)

package available at https://github.com/agentmess/Spectral-Spatial-RF-Pulse-Design and described in Ref. 12 to facilitate the design of these pulses. With SPSP RF pulses, the primary trade-off is between spectral bandwidth versus spatial selectivity and slice thickness. The spectral selectivity is determined by the pulse duration for both spectral and SPSP RF pulses.

Spectral and SPSP RF pulses can either be designed to excite just a single resonance frequency ('single-band') or multiple frequencies ('multiband'), depending on the acquisition strategy. Examples of SPSP single-band and multiband pulses are shown in Figure 4. Single-band pulses can be used with fast imaging readouts (see section titled 'Metabolite-specific Imaging'), while multiband pulses can be used with magnetic resonance spectroscopic imaging (MRSI) or model-based strategies, both described in later sections.

Transverse Excitation Field (B_1) Calibration

Without accurate calibration of the transverse field (B_1), any RF pulse strategy will not behave as expected. VFA strategies, whether based on constant or maximum SNR, can deviate considerably from the expected signal response. In single time-point experiments, this can result in increased image blurring.

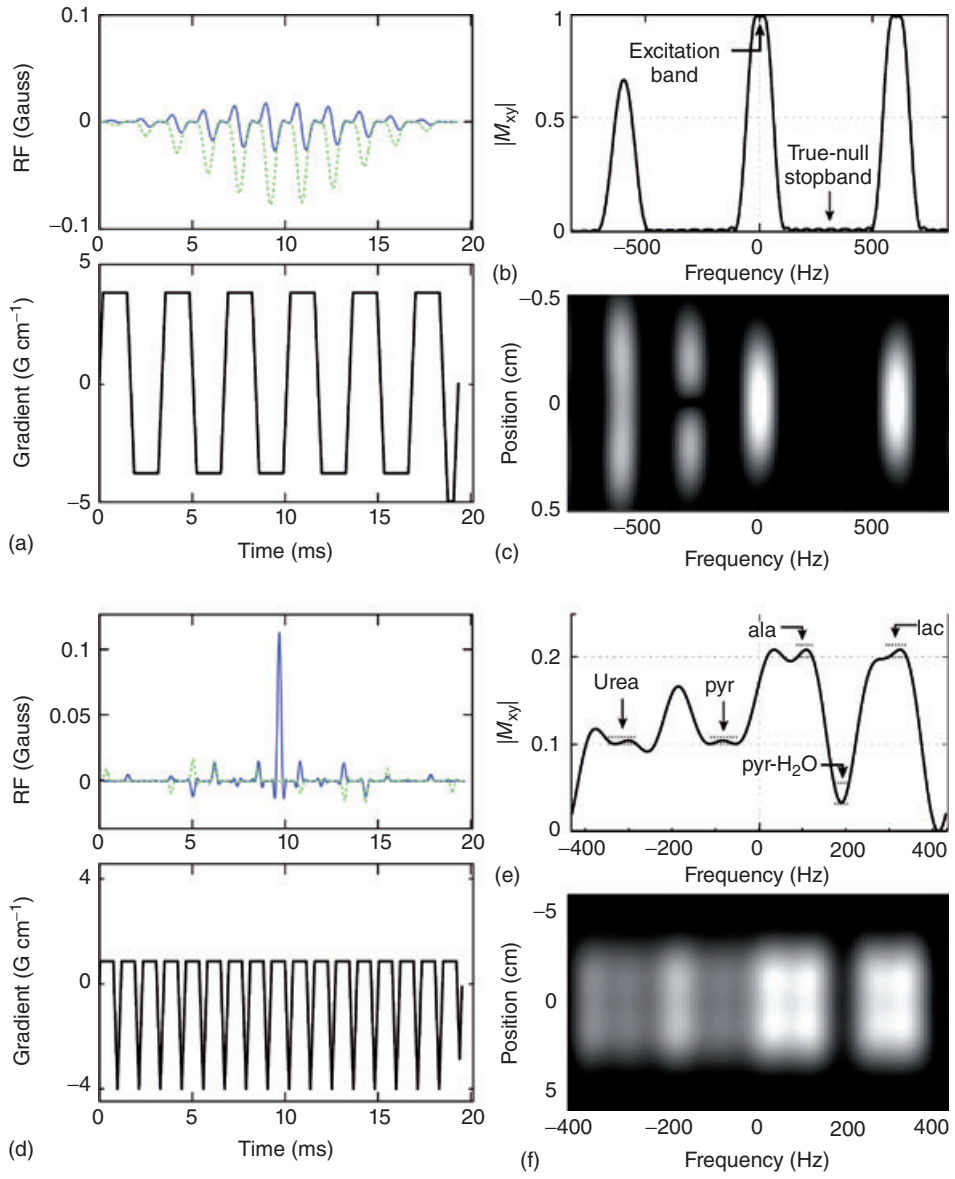

Figure 4. Example of spectral-spatial (SPSP) RF pulses designed for HP ^{13}C studies. (a–c) Single-band excitation pulse using a symmetric echo-planar gradient, designed for two-dimensional (2-D) metabolite-specific imaging. The design parameters include 90° flip angle, 5 mm slice thickness, and a frequency profile that only excites lactate or pyruvate, depending on the choice of center frequency at 3 T. (d–f) A multiband excitation pulse using a flyback echo-planar gradient, designed for three-dimensional (3-D) dynamic MRS imaging (MRSI) with copolarized pyruvate and urea. The design parameters include 6° (urea, pyruvate) and 12° (lactate and alanine) flip angles, and a 4 cm slab thickness at 3 T

In dynamic experiments, a nonuniform or miscalibrated B_1 will lead to errors in the kinetic modeling and inefficient usage of the HP magnetization. B_1 calibration is challenging in HP MRS because there is typically insufficient natural abundance signal from the non-proton nuclei to use standard MR pre-scan calibrations. Some options for B_1 calibration in non-proton HP MRS studies include using (1) separate phantom scans, (2) placing phantoms near the subject, or (3) using the HP magnetization itself:

1. For a given RF coil configuration that is relatively static and consistent between phantom and in vivo studies, an approximate B_1 calibration can be performed using enriched phantoms prior to the in vivo HP MRS. This may not account for loading variations between different experiments or dynamic changes between the calibration and the in vivo experiment.
2. Enriched phantoms placed next to the object of interest can also be used, and were applied in the first-in-man clinical trial of HP ^{13}C-pyruvate.[6] The limitation of this method is that it only provides a measurement of the B_1 field at the phantom location outside of the object.
3. B_1 calibration can be performed after administration of the HP agent. This uses some of the available HP magnetization, but can account for variability between subjects and experiments. The Bloch–Siegert shift method

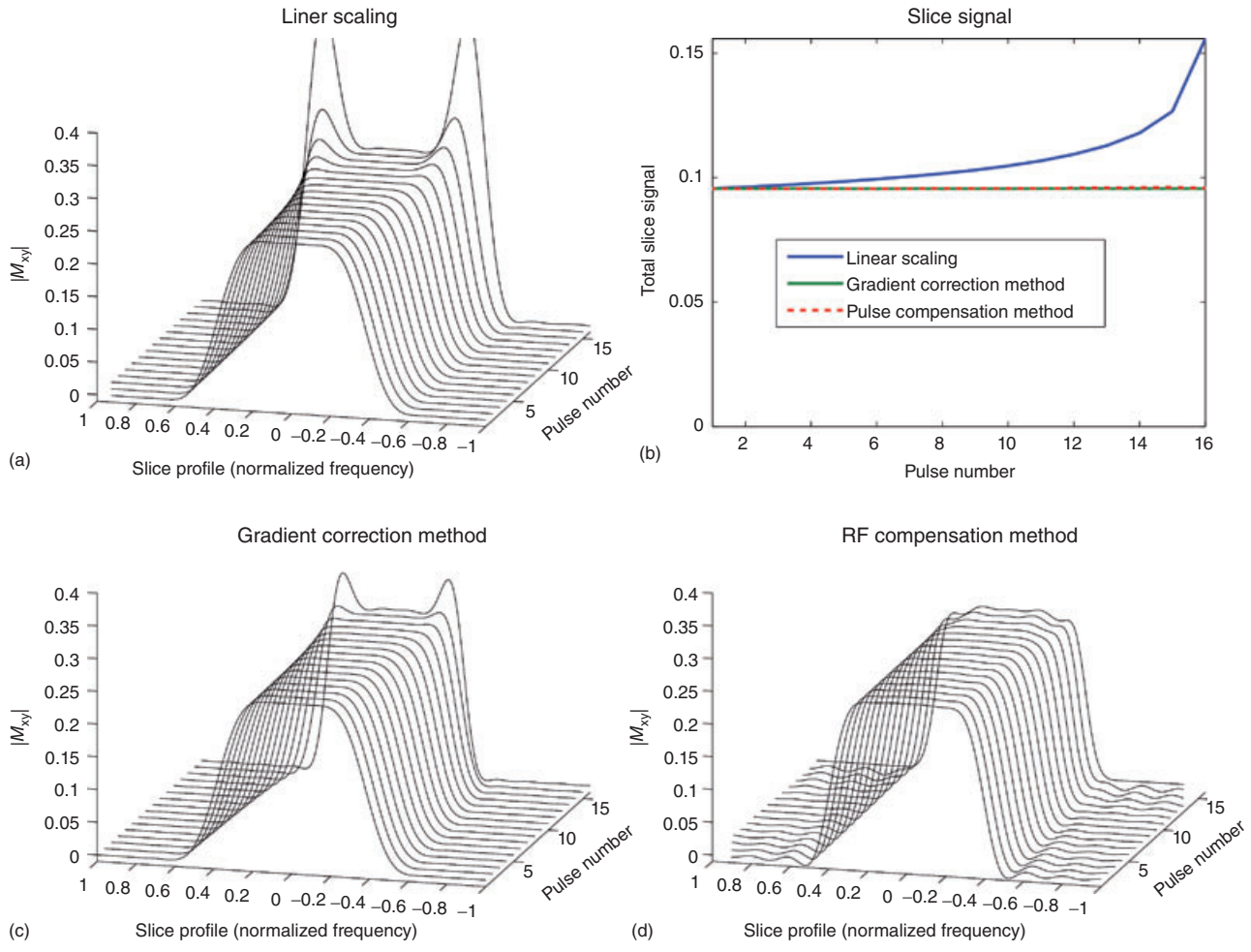

Figure 5. Simulated slice profile evolution of HP magnetization over repeated application of RF pulses with an RF-compensated VFA schedule (equation (5) with $N = 16$), neglecting T_1, metabolic conversion and flow effects. (a) Nominally, with linear scaling of the RF pulses, the slice profile becomes broader and eventually develops 'wings' of elevated signal at the edges of the slice profile, (b) which results in inadvertently increasing the total slice signal in later pulses (blue curve). (c) This effect can be compensated for by increasing the slice-selection gradient, decreasing the slice thickness for later RF pulses[20]; or (d) completely corrected by designing compensated RF pulses.[21] Both approaches result in constant total slice signals (part b, green and red curves)

is very efficient and accurate for B_1 mapping and has been successfully applied to HP MRS applications.[18,19]

Slice Profile Effects

When using spatially selective RF pulses in HP MRS experiments, there are two main sources of errors: chemical shift slice misregistration (or chemical shift displacement artifact; see ***Single-Voxel MR Spectroscopy***), and slice profile distortions following the application of multiple RF pulses.

Chemical shift slice misregistration results in different spatial displacements of slices being excited for different metabolites, and is especially problematic if there are large chemical shift frequency differences between compounds. The spatial slice displacement, δz, is determined by the spectral separation of compounds, δf, in combination with either the slice selection gradient strength, G_z, or the RF pulse bandwidth, $\mathrm{BW_{rf}}$, and slice thickness, Δz:

$$\delta z = \frac{\delta f}{\gamma/2\pi\dot{c}G_z} = \frac{\delta f}{\mathrm{BW_{rf}}}\Delta z \qquad (8)$$

In an SPSP RF pulse design, the chemical shift slice misregistration can be corrected to some extent. A method for this correction can be found in the MATLAB SPSP RF pulse design package, which accounts for the nonuniform k-space (k_z) – time sampling by solving a least-squares problem.[12]

Repeated application of spatially selective RF pulses in HP experiments also results in distortion of the slice profile (Figure 5). Due to the unavoidable imperfections in the slice profile, the HP magnetization will generally experience unequal depletion of magnetization across the entire slice profile. This can lead to substantial modifications of the received signal slice profile, particularly with large numbers of RF pulses, large flip angles, and/or typical VFA schemes.[20] The signal summed across the slice is inadvertently increased with later RF pulses, which can lead to image distortions, inaccurate kinetic model fitting, and more. A simple but imprecise solution to compensate for the slice signal distortions is to decrease the slice thickness for later RF pulses ('Gradient Correction Method' in Figure 5c).[20] The slice profile distortions can also

be addressed by designing a set of RF pulses that includes compensation for magnetization depletion by previous RF pulses ('RF Compensation Method' in Figure 5d),[21] which preserves the slice profile. However, both of these methods do not account for decay, metabolic conversion, or flow, all of which are largely unknown prior to the experiment. Another solution is to incorporate the known slice profile distortions into the image analysis, for example, kinetic modeling.

Acquisition Strategies

Data acquisition strategies in HP MRS experiments must account for the chemical shifts expected, efficiently utilize the nonrenewable HP magnetization, and acquire data quickly relative to perfusion, uptake, metabolism, and relaxation decay processes. Studies of inert HP molecules, such as ^{13}C-urea or water, for the most part can utilize rapid and efficient conventional MRI strategies combined with the HP RF pulse strategies described. Studies of metabolically active HP molecules require spectral resolution to separate metabolites. If imaging is not required, then FID or spin-echo MRS acquisitions combined with HP RF pulse strategies will suffice.

In this section, we focus on acquisition strategies in HP metabolic imaging experiments involving multiple compounds, where the pulse sequences must not only have spatial encoding but spectral encoding as well. We have included three major categories of pulse-sequence strategies for obtaining HP metabolic imaging data: MRSI,[22,23] model-based multi-echo approaches,[24–26] and metabolite-specific imaging.[27,28] This section also discusses strategies for accelerated imaging, including compressed sensing and parallel imaging, and ultrafast two-dimensional (2-D) MRS methods for HP agents.

Spectroscopic Imaging

Phase-encoded MRSI is routinely used in HP experiments because it is robust, and provides a large spectral bandwidth and high spectral resolution. However, the spectra in HP studies, particularly HP ^{13}C, are often sparse with metabolites separated by >3 ppm, which lessens the need for high spectral resolution. Furthermore, performing MRSI with phase encoding on all axes requires at least $N_x \times N_y$ RF excitations for 2-D MRSI, where $N_x \times N_y$ is the number of voxels in the 2-D spatial array. Even a coarse 8×8 matrix requires 64 RF excitations that would typically result in an acquisition time (5–10s or more) for one image that would not allow subsequent measurements of metabolite reaction dynamics. Phase-encoded MRSI will find more utility in HP experiments with complicated spectra or when there is a large chemical shift dispersion between substrate and product and where dynamic studies are of lesser concern, such as in certain [2-^{13}C]pyruvate experiments, where the large spectral bandwidth and high spectral resolution afforded by phase-encoded MRSI is a key advantage.

Rapid spectroscopic imaging techniques employing switched time-dependent or echo-planar (EPI)-type gradients applied during acquisition can greatly reduce the scan time and RF deposition for HP experiments compared to phase-encoded MRSI. Joint spectral and spatial encoding is accomplished by traversing k-space at multiple TEs, shifted in time by ΔTE (Figure 6). By acquiring the same k-space point (k_x, k_y) at multiple TEs, a Fourier transform (FT) along the echo dimension can produce a spectrum at each k-space point, which in turn can be transformed into the spectroscopic image. However, the resulting speed advantage comes at a cost of a more limited spectral bandwidth (SBW $\approx 1/\Delta$TE), spatial resolution, and SNR efficiency. To increase the spectral bandwidth, all of these rapid spectroscopic imaging k-space trajectories can be interleaved by echo shifting and/or rotating the trajectory, albeit at a cost of increased scan time and RF power deposition. It is important to note that, compared to ^{1}H, the low-gyromagnetic ratio of nuclei such as ^{13}C (1/4th that of ^{1}H) increases the demand on gradient strength and slew rate, requiring the gradients to work four times as hard to achieve the same scan parameters. This is particularly problematic at higher B_0 because the chemical shift difference in Hertz between metabolites scales linearly with field strength, so that even higher bandwidths must be accommodated.

The spectral and spatial encoding for rapid MRSI techniques with switched gradients can be achieved with several k-space trajectories, including echo-planar spectroscopic imaging (EPSI),[30] radial,[31] spiral,[32] and concentric rings,[29] all of which reduce the number of excitations, the scan time, and RF power deposition compared to phase-encoded MRSI. It is important to note that by encoding in the spectral dimension, non-Cartesian trajectories that might normally be sensitive to off-resonance artifacts are rendered amenable to MRSI. The trade-off between these parameters for different rapid MRSI strategies is shown in Figure 6.

EPSI eliminates the need for one of the phase-encoding dimensions and is robust to many system imperfections. It offers a relatively straightforward implementation and reconstruction, as it is very similar to the EPI k-space trajectory commonly used in MRI. The EPSI spatial-encoding dimension is identical to the frequency-encoding dimension in MRI, and thus should correspond to the longest field-of-view (FOV) dimension for the largest acceleration gain. There are generally two EPSI sampling strategies: flyback, in which data are acquired only when going one direction in 2-D k-space, and symmetric, where data are acquired while traversing both directions in k-space (see Figure 6). Flyback EPSI is very robust but has limited SNR efficiency, while symmetric EPSI offers the best SNR efficiency and imaging speed but at the expense of increased sensitivity to system imperfections such as eddy currents.

Of the non-Cartesian rapid MRSI trajectories, spiral MRSI is the most efficient to date at traversing k-space, and typically requires the fewest number of excitations. In a single interleave, it has a very long ΔTE and thus a low SBW, but it can be favorably interleaved to increase the SBW (Figure 6). Spiral trajectories are inherently very sensitive to system imperfections such as eddy currents, resulting in increased artifacts compared to EPSI or phase-encoded MRSI.[33] As gradient systems and compensation algorithms improve, this may become less of an issue. The concentric ring trajectory provides speed improvements over EPSI, but without the sensitivity to

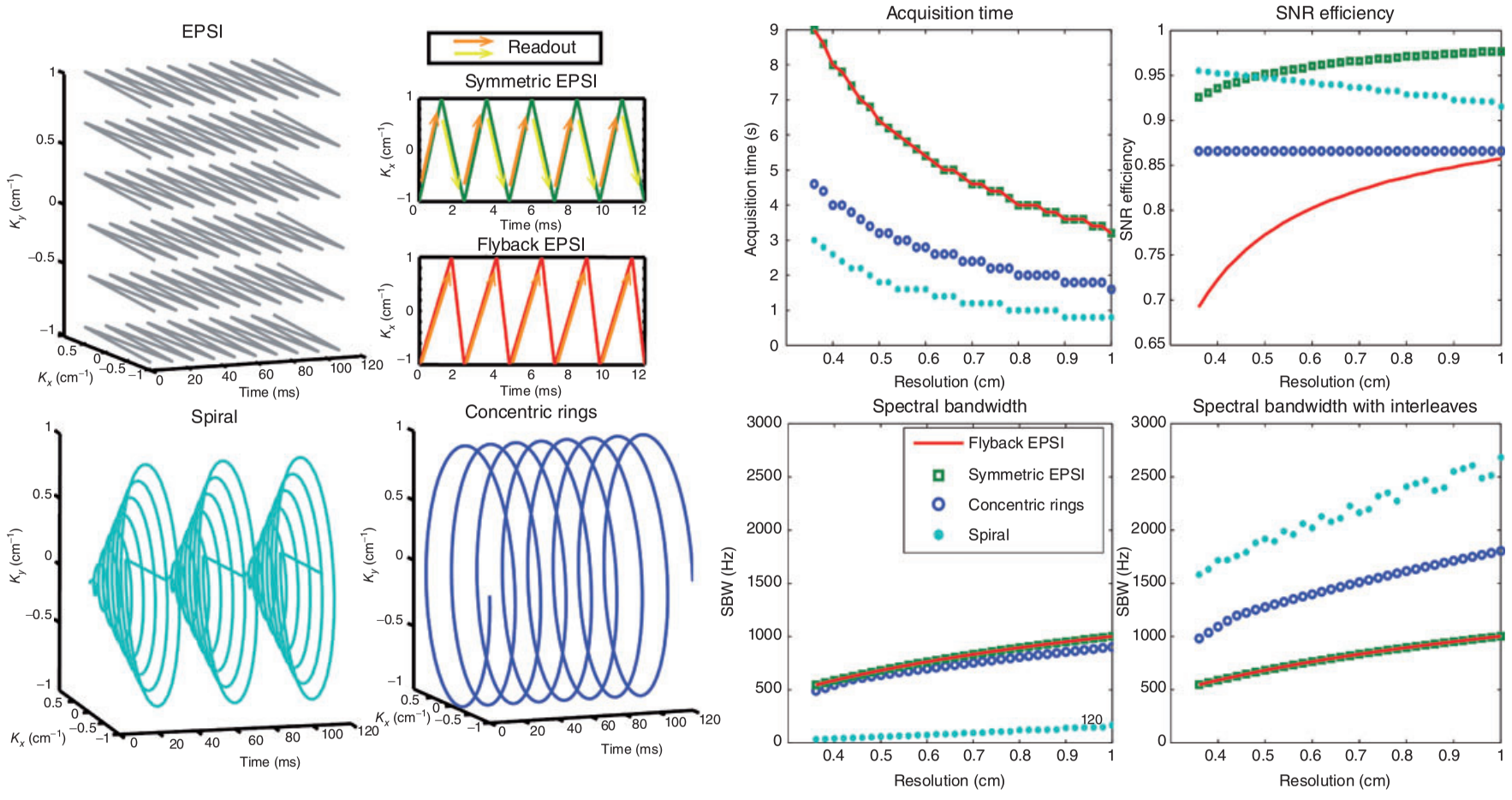

Figure 6. Illustration and comparison of several rapid MRSI methods employing switched/time-dependent read-out gradients. Left two columns: image *k*-space trajectories for EPSI (symmetric and flyback), spiral and concentric rings spectroscopic imaging. Right two columns: Design trade-offs between spatial resolution, spectral bandwidth, acquisition time, and SNR efficiency, assuming typical clinical MRI system gradients with a maximum amplitude of 40 mT m^{-1} and a maximum slew rate of 150 mT m^{-1} ms^{-1}. EPSI is the slowest, but symmetric EPSI trajectories have very high SNR efficiency. The concentric rings method requires half of the total acquisition time compared with the EPSI trajectories, offers about 87% SNR efficiency, and provides much wider SBW than flyback EPSI and symmetric EPSI. Although spirals are nominally the most efficient trajectories (offering the best acquisition time and SBW benefit while sacrificing the least SNR), they are limited by their susceptibility to gradient infidelities. (Reproduced with permission from Ref. 29. © John Wiley & Sons Ltd., 2014)

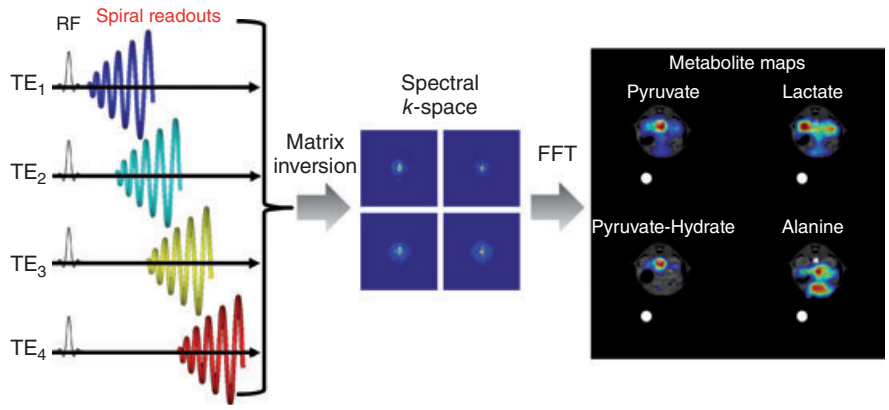

Figure 7. Schematic illustrating the acquisition and reconstruction of a model-based spiral acquisition. In this illustration, data are acquired with a long-duration readout spiral that is spoiled at each TR. Subsequent excitations are shifted in time by ΔTE. For non-Cartesian approaches, the matrix decomposition occurs in *k*-space, yielding *k*-space data for each metabolite. A subsequent gridding or nonuniform fast FT (nuFFT) step yields spectral images for each hyperpolarized metabolite

gradient infidelity of spiral MRSI. It requires half the number of excitations compared to EPSI for a square FOV since it encodes each TR interval in two spatial dimensions. It also has reduced motion and flow artifacts while maintaining the robustness of flyback EPSI to system imperfections. Radial MRSI requires more excitations than EPSI because it oversamples the center of *k*-space and has identical SNR efficiency as concentric rings at 87%. It is used because it provides reduced sensitivity to motion and flow artifacts due to the repeated sampling of the center of *k*-space. This repeated sampling could also be used for motion correction or evaluating data quality. All of these non-Cartesian rapid MRSI trajectories can be reconstructed using similar algorithms applied to non-Cartesian MRI such as gridding[34] or the nonuniform fast FT (nuFFT[35]; see also ***CSI and SENSE CSI***; ***High-Speed Spatial–Spectral Encoding with PEPSI and Spiral MRSI***).

Model-based Approaches

As an alternative, model-based techniques can be combined with MRSI to further reduce the RF deposition and imaging requirements. HP ^{13}C spectra are amenable to model-based techniques[24] because of the readily available prior knowledge of the number and relative frequency of ^{13}C resonances. In this approach, multiecho data are acquired in a manner similar to conventional EPSI or spiral MRSI, but fewer echoes are required because of the prior knowledge of the number and frequency difference of the HP spins (Figure 7). In these approaches, at least $N+1$ echoes are required to solve for N metabolites. Unlike the conventional MRSI techniques enumerated above, optimally chosen echo times (TEs) will prevent aliased peaks from overlapping without the need to fully sample the spectral dimension. This reduces the number of echoes required for spectral encoding, further reducing RF deposition and scan time.

In these approaches, the signal can be modeled in either image space or *k*-space. The domain to solve for the metabolite maps will ultimately depend on the trajectory used because of the nature of off-resonance artifacts. For a Cartesian approach, the metabolite maps can be solved directly in image space on a voxel-by-voxel basis. The signal model from N species at the nth TE can be written in image space as[24]

$$S(\mathrm{TE}_n) = \left(\sum_{i=1}^{N} \rho_i e^{2\pi i \Delta f_i \mathrm{TE}_n} \right) e^{2\pi i \psi TE_n} \qquad (9)$$

Here, the signal in a voxel is the sum of the spin density of each metabolite, with a phase accrual given by the chemical shift differences (Δf_i) and B_0 field inhomogeneities (ψ). With the known phase accrual due to chemical shift, the goal is to solve for each unknown metabolite map ρ_i. The outer field map term in equation (9) renders the system nonlinear and can be estimated from the HP data by using an iterative solver in much the same way that conventional ^{1}H fat-water IDEAL (iterative decomposition with echo asymmetry and least-squares estimation) method[36] operates. A more straightforward approach is to estimate the field-map from ^{1}H data. With a known field map scaled by the ratio of the gyromagnetic ratios of the HP nucleus to that of ^{1}H to account for the difference in Larmor frequency, the outer phase term can be demodulated and the metabolite maps solved for on a voxel-by-voxel basis using a Penrose–Moore pseudoinverse.

Off-resonance artifacts manifest differently for Cartesian and non-Cartesian trajectories. With a Cartesian acquisition, off-resonance will manifest as a shift in the readout direction and can be solved in image space. As long as the read-out bandwidth is sufficiently large (at least twice the frequency shift of HP metabolites), any off-resonance will result in a sub-voxel shift in image space. In contrast, off-resonance in non-Cartesian acquisitions manifests as blurring that becomes worse as the readout duration increases. This is an issue for HP ^{13}C imaging, since the long inhomogeneously broadened spin–spin relaxation (T_2^*) times of most metabolites result in an optimum readout duration on the order of 50 ms.[37] While matrix decomposition in image space can recover the individual metabolite maps, it does not account for or correct blurring due to differences in chemical shift frequencies. Instead, the matrix decomposition must occur in *k*-space, either on a

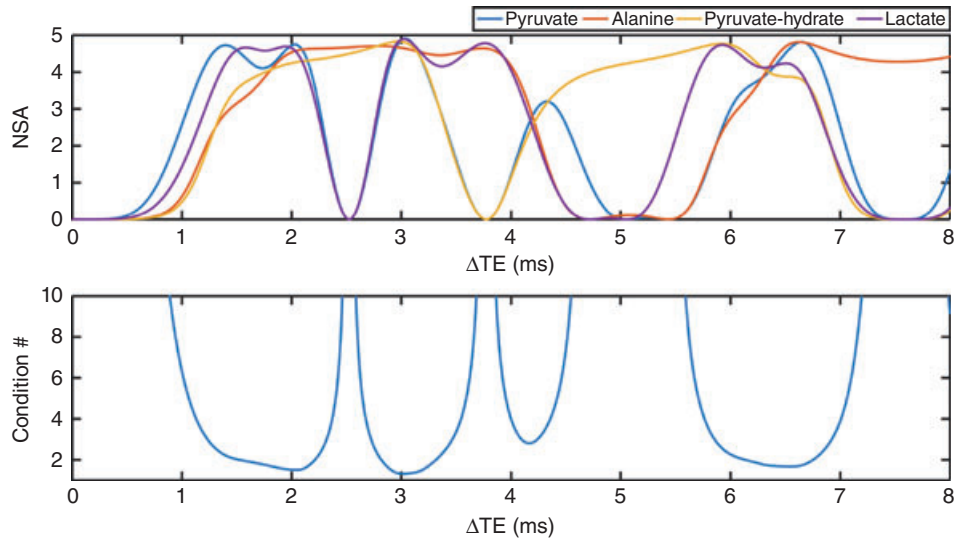

Figure 8. Number of signal averages (NSA) and condition number as a function of echo spacing (ΔTE) for pyruvate and its metabolic products at 3 T for 5 acquired echoes. Local minima in the NSA plot are indicative of TEs that are in-phase for all echoes and correspond to echo spacings equal to a full period ($1/\Delta f$). Optimal noise performance is achieved for an echo spacing that yields an NSA equal to the number of echoes, allowing for sufficient phase accrual at all echo times

point-by-point basis along the readout direction,[25,38] or by jointly solving in both spectral and spatial domains.[26] Ignoring the field-map term, the signal $S_n(\vec{k})$ at a k-space point, $\vec{k}$, for the nth echo can be modeled in k-space as[25,38]

$$S_n(\vec{k}) = \sum_{i=1}^{N} \rho_i(\vec{k}) e^{2\pi i \Delta f_i (\mathrm{TE}_n + \tau(\vec{k}))} \quad (10)$$

In this nomenclature, $\tau(\vec{k})$ is the relative acquisition time of each k-space sample within the readout trajectory, not including the echo time, as TE_n accounts for the different TE acquisitions. Following point-by-point matrix decomposition in k-space, the metabolite k-space data can be interpolated onto a Cartesian grid and subsequently Fourier transformed. By performing the matrix decomposition in k-space, phase accrual due to chemical shift differences are properly accounted for and off-resonance blurring is minimized.

However, choosing an optimal echo spacing is crucial to the image quality and SNR in a model-based approach. Unlike the conventional MRSI techniques described in the section titled 'Spectroscopic Imaging', where Nyquist sampling criteria must be met to prevent spectral aliasing, optimally chosen TEs can result in controlled aliasing that will not affect the decomposition of the spectral peaks. The echo spacing can be optimized by calculating the effective number of signal averages (NSA) for each ^{13}C metabolite.[24] NSA is a measure of relative SNR for each metabolite and is a function of chemical shift and sampled TEs (Figure 8):

$$\mathrm{NSA}_i = \frac{1}{\mathrm{diag}_i((A^H A)^{-1})} \quad (11)$$

$$A_n^i = \exp(i2\pi \Delta f_i TE_n) \quad (12)$$

Here, Δf_i is the relative frequency difference between metabolites and H denotes the Hermitian transpose. At maximum, the NSA for the ith species will equal the number of acquired echoes. NSA decreases when there is insufficient phase accrual between echoes, and local minima will occur when the echo spacing is equal to a full period ($1/\Delta f$). This corresponds to the case when the echoes are in-phase at each TE, which can also be conceptualized as having two peaks alias on top of each other.

As an alternative to NSA, the condition number of the matrix $\boldsymbol{A}$ could also be calculated. While it is a more straightforward calculation, the condition number will only provide a measure of noise performance of the system as a whole, whereas NSA is more elucidating because it permits noise optimization on a metabolite-specific basis. This could be useful when choosing an echo spacing that maximizes NSA for a low-concentration metabolite at the expense of noise amplification of the injected substrate, for instance. (For additional information on model-based methods, see also ***Direct Water–Fat Imaging Methods: Chemical Shift-Selective and Chemical Shift-Encoded MRI***.)

Metabolite-specific Imaging

In many instances the HP spectrum consists of well-separated resonances, such as [1-^{13}C]pyruvate and its metabolites. For these cases, selective excitation of a single resonance followed by a fast MRI readout[27,28] can be an extremely rapid and SNR-efficient approach. With only one metabolite encoded per excitation, an efficient, long-duration readout can take full advantage of the long T_2^* of HP metabolites to maximize SNR efficiency. For this purpose, rapid, RF-efficient MRI techniques employing spirals or an EPI readout are a natural choice for pulse sequence design.

In these approaches, a single-band SPSP RF pulse is used to excite a single metabolite (Figure 4a–c), followed immediately by the readout module. The center frequency is then shifted by Δf to excite the next metabolite, and this process

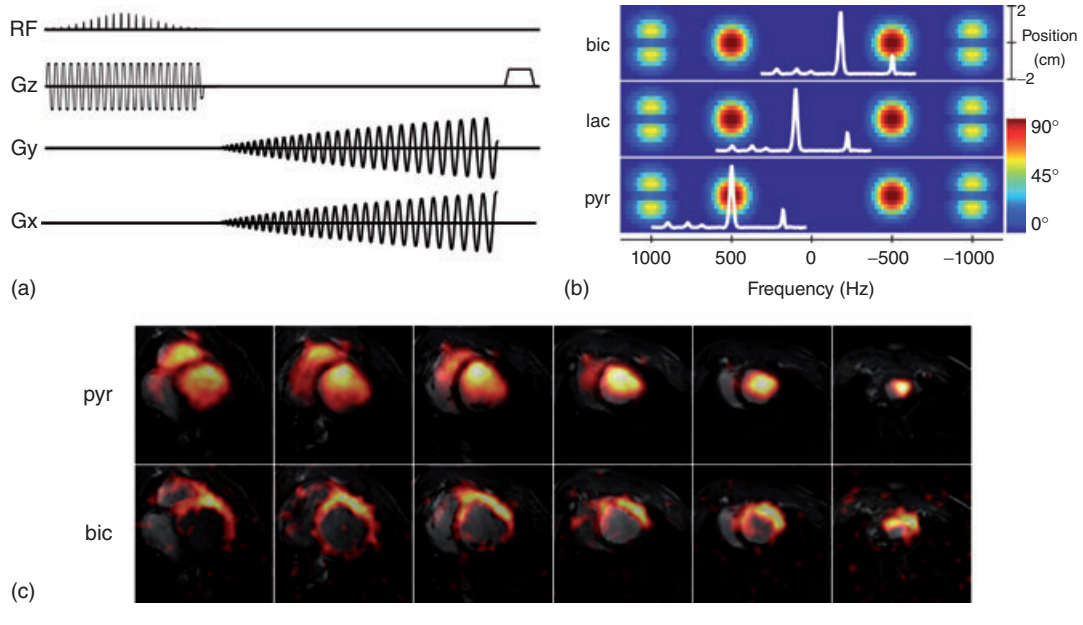

Figure 9. (a) A metabolite-specific MRI pulse sequence consisting of a single-band SPSP excitation pulse followed by a fast imaging readout, such as EPI or spirals (illustrated here). (b) In order to generate images of multiple metabolites, the center frequency of the SPSP pulse can be changed between TRs such that a passband excites a different metabolite each time. In this example, the pulse frequency is shifted to excite ^{13}C-bicarbonate (bic), [1-^{13}C]lactate (lac) and [1-^{13}C]pyruvate (pyr) (reproduced with permission from Ref. 28. © John Wiley & Sons Ltd., 2010). This approach allows for rapid MRI and thus can be applied to multislice cardiac metabolic imaging, as shown in (c) (reproduced with permission from Ref. 28. © John Wiley & Sons Ltd., 2010). In this example, six slices were acquired with 8.8 mm in-plane resolution and 1 cm thickness within a single breath-hold (18 s) in a pig model: pyruvate in the blood pool and bicarbonate in the myocardium are clearly depicted

is repeated until all of the desired metabolites have been encoded, as illustrated in Figure 9. The readout module consists of a fast imaging readout, such as EPI or spirals, which can be reconstructed using established techniques from conventional MRI.

While a long readout duration improves SNR efficiency, it also results in images that are sensitive to off-resonance phase accrual. Even though the single-band SPSP pulse is designed with a narrow passband, phase accrual due to field inhomogeneities can severely degrade image quality, either as a shift in the EPI 'blip' direction or as blurring in a spiral readout. So-called autofocus algorithms[28,39,40] can be used to correct for this unwanted phase accrual in spiral readouts, thereby mitigating blurring and improving image quality. The large difference in signal between the injected substrate and downstream metabolic products can be addressed by exciting with independently adjusted metabolite flip angles, as described in the section titled 'RF Pulse Strategies',[12,13] which leads to a more efficient use of the magnetization.

SPSP pulses are also inherently sensitive to spectral separation and field inhomogeneities. Having sufficient spectral separation (in Hertz) between metabolites is crucial so that the SPSP pulse duration is not inordinately long, which makes their use difficult for low-field ($\leq$1.5 T) systems. Even at higher fields ($\geq$3 T), a long pulse duration can be required for a narrow passband (typically 10–15 ms for ^{13}C at 3 T). This increases the minimum TE, which in turn reduces the SNR due to T_2^* signal decay when employing gradient-echo approaches. Furthermore, the narrow passbands required for spectral selectivity make these pulses sensitive to B_0 inhomogeneities and incorrect center frequency settings that may result from operator or calibration errors. Imaging near air–tissue interfaces or using clinical scanners that lack adequate high-order shimming may pose difficulties for this approach over larger FOVs due to the B_0 sensitivity.

SSFP-based Approaches

Steady-state free precession (SSFP)-based approaches have very high SNR efficiency and are appealing for HP MRS studies. This high efficiency is because balanced steady-state free precession (bSSFP) sequences refocus residual transverse magnetization between TRs, whereas most other sequences use gradient spoiling to destroy any residual transverse magnetization at the end of each TR. This is achieved in bSSFP by refocusing all gradients within the TR. The main disadvantage of bSSFP is its sensitivity to off-resonance effects: its signal profile as a function of frequency has periodic nulls at intervals of 1/TR, which result in signal voids known as banding artifacts. Furthermore, when multiple resonance frequencies from different chemically shifted metabolites are present, some frequencies may fall on these nulls or their signal intensities may be modulated, potentially confounding quantification. However, for single-resonance frequencies (e.g., HP perfusion tracers such as ^{13}C-urea), standard bSSFP sequences can be readily applied.[41–43] In these applications, the lower gyromagnetic ratios of non-proton HP compounds will result in less off-resonance due to B_0 inhomogeneities, reducing banding artifacts; but they will also require longer TRs for the same

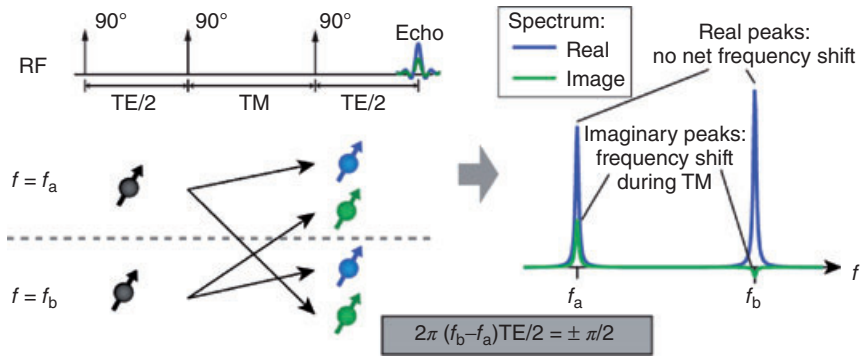

Figure 10. Illustration of the MAD-STEAM exchange spectroscopy approach[50]. The TE is chosen such that exchanging spins (green) have a net phase shift of $\pm \pi/2$, whereas nonexchanging spins (blue) have no phase shift. These can be separated by reconstructing a complex spectrum, where nonexchanging spins will be in the real channel and exchanging spins will be in the imaginary channel. Accurate phasing is essential for this method, which can be achieved by copolarizing inert ^{13}C-urea to serve a localized phase reference in [1-^{13}C]pyruvate HP experiments. (Reprinted from J Magn Reson, 225C, P. E. Z. Larson, A. B. Kerr, C. Leon Swisher, J. M. Pauly and D. B. Vigneron, A rapid method for direct detection of metabolic conversion and magnetization exchange with application to hyperpolarized substrates, 71.[50]. © 2012, with permission from Elsevier)

resolution as a comparable ^{1}H scan, which in turn increases the likelihood of banding artifacts.

For HP studies with multiple resonance frequencies, several bSSFP approaches have been proposed. Acquiring multiple echoes within each TR with bSSFP allows for a model-based separation (see section titled 'Model-based Approaches') of metabolites in HP studies.[44] This requires a very careful and limited choice of TR and TE values to avoid banding while enabling separation of the metabolites. Using low-flip angles with bSSFP results in a frequency profile with a narrow excitation band every 1/TR, and this profile has been used for metabolite-specific imaging at 14.1 T.[45] Such an approach requires careful choice of TR, is limited in flip angle, and is sensitive to off-resonance effects. Another method is to increment the RF pulse phase between TRs to effectively map the frequency response and eliminate off-resonance artifacts.[46] However, the resulting extended acquisition negates some of the efficiency benefits of SSFP. In general, no SSFP approach has emerged as a robust candidate for HP studies, although there is great potential given their high SNR efficiency.

2-D MRS

2-D NMR/MRS experiments are useful for measuring interactions between spins such as coupling and exchange (see ***High-Speed Spatial–Spectral Encoding with PEPSI and Spiral MRSI***). In equilibrium, 2-D MRS experiments typically require large numbers of readouts with high flip angle excitations, which are unsuitable for HP substrates. These could simply be modified to use a constant small or VFA schedule, in order to be applied to HP substrates.[47] However, a more elegant and efficient solution is to use ultrafast 2-D MRS methods[48,49] that accelerate the experiment by encoding the indirect time dimension spatially. This allows for single-shot 2-D MRS experiments with HP substrates. Another approach known as MAD-STEAM (Metabolic Activity Decomposition Stimulated Echo Acquisition Mode) uses undersampling of the indirect time dimension along with phase referencing to perform rapid 2-D EXSY with HP substrates (Figure 10).[50] This approach has been shown to provide more quantitative measures of enzyme kinetics in HP pyruvate experiments in vivo, by directly measuring the metabolic conversion and eliminating confounding factors such as signal from vascular metabolites.[51]

Acceleration Strategies

It is challenging to capture the rapidly decaying signal and metabolic conversion in HP MRS, particularly when multiple TRs are required for spatial localization. For this reason, HP MRS can benefit greatly from the accelerated acquisition methods such as compressed sensing and parallel imaging used in state-of-the-art MRI. Furthermore, if the unaccelerated acquisition times are long relative to T_1 or metabolic conversion (Figure 11), then accelerated acquisitions can reduce the losses due to these factors during the acquisition and so increase the SNR.[52]

Compressed Sensing. HP MRS is particularly well suited for compressed sensing[53] because experimental methods can be designed to fulfill the key requirements of: (i) having sufficient SNR for acceleration (provided by the hyperpolarization and VFA strategies); (ii) having signal sparsity in some domain (typically in the spectral dimension, but also in spatial dimensions); (iii) being amenable to pseudorandom k-space sampling strategies that create incoherent aliasing in the sparsity domain; and (iv), incorporating nonlinear reconstruction methods.

Compressed sensing can theoretically be integrated into all of the acquisition strategies described. For example, consider an HP MRSI implementation using pseudorandom blip gradients that are applied during an EPSI readout (Figure 12).[54,55] The blip gradients lead to a pseudorandom, sparse sampling in $k_x - k_y - k_f$ space that has incoherent aliasing in the sparse domain (the frequency dimension with its limited peaks). The compressed sensing reconstruction then exploits this sparsity to reconstruct a fully sampled dataset. Variable density sampling in $k_x - k_y$ with denser sampling in the center of k-space is used because it provides improved SNR with minimal additional scan time. This strategy can also be extended to dynamic

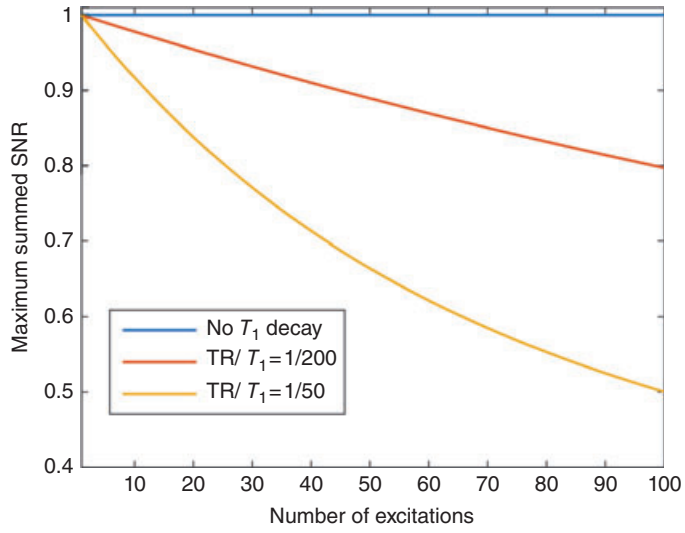

Figure 11. The maximum total HP SNR achievable with optimal variable flip angle strategies [equation (7)] decreases as T_1 decay becomes substantial across multiple excitations. For this reason, it is advantageous to use accelerated acquisitions

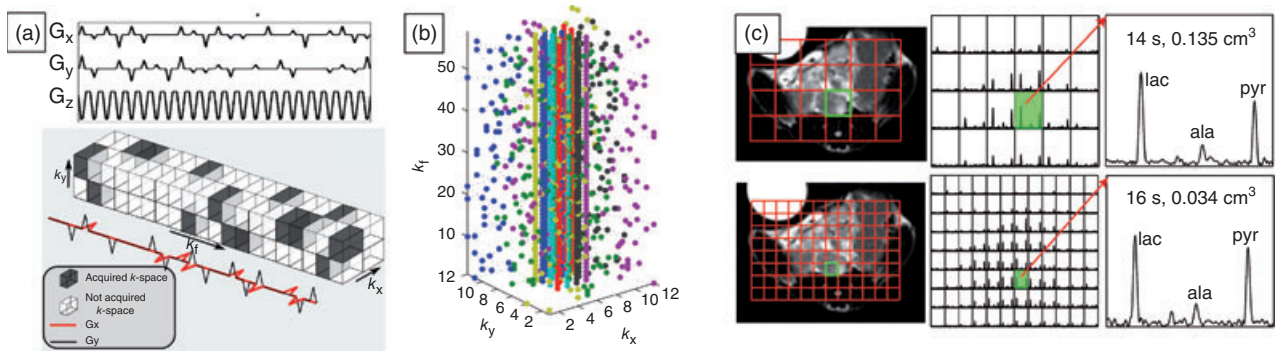

Figure 12. Implementation of compressed sensing with EPSI. (a) Pseudorandom blip gradients are applied during the EPSI readout. (b) Combining multiple TRs (different colors) with this readout results in pseudorandom, sparse sampling in $k_x - k_y - k_f$ space that provides incoherent aliasing required for compressed sensing. (c) Example of HP ^{13}C-pyruvate (pyr) administration in a transgenic prostate tumor mouse model showing that this compressed sensing implementation (bottom) can provide a fourfold reduction in voxel size in a similar scan compared to a fully sampled MRSI (top), with spectra from the green-shaded voxels expanded at right (lac = lactate; ala = alanine). Adapted from Refs 54, 55

imaging where the relatively smooth dynamics can also be exploited for further acceleration.

Parallel Imaging. Parallel imaging can, in principle, also be integrated into all of the acquisition strategies described. It requires an RF receiver coil array, and exploits the spatial localization information provided by these different coils in order to accelerate the acquisition by a factor of R. Interestingly, the SNR in HP parallel imaging performed with VFAs does not suffer from the usual acceleration penalty of $\sqrt{R}$ in thermal equilibrium acquisitions.[52] However, there is still SNR loss due to the g-factor (geometric factor) when using parallel imaging with HP agents that depend on the coil geometry, object geometry, sampling pattern, and reconstruction method:

$$\mathrm{SNR}_{\mathrm{PI}} = \mathrm{SNR}/g \qquad (13)$$

The key challenge for HP parallel imaging is that calibration of the receiver coil sensitivities is required for reconstruction. For conventional studies where the magnetization is in thermal equilibrium, sensitivity maps can be directly measured. However, for HP studies, there is typically insufficient natural abundance signal prior to injection of the HP agent to provide a sensitivity map. For this reason, autocalibrated parallel imaging methods such as GRAPPA are desirable.[56] These require additional measurements of the center of k-space for calibration which reduces the overall acceleration, but does allow for accurate coil sensitivity calibration (as demonstrated in Figure 13). Recently introduced calibration-less methods may remove the requirement for such additional measurements while still providing the necessary coil sensitivity information[58] (see also ***CSI and SENSE CSI***).

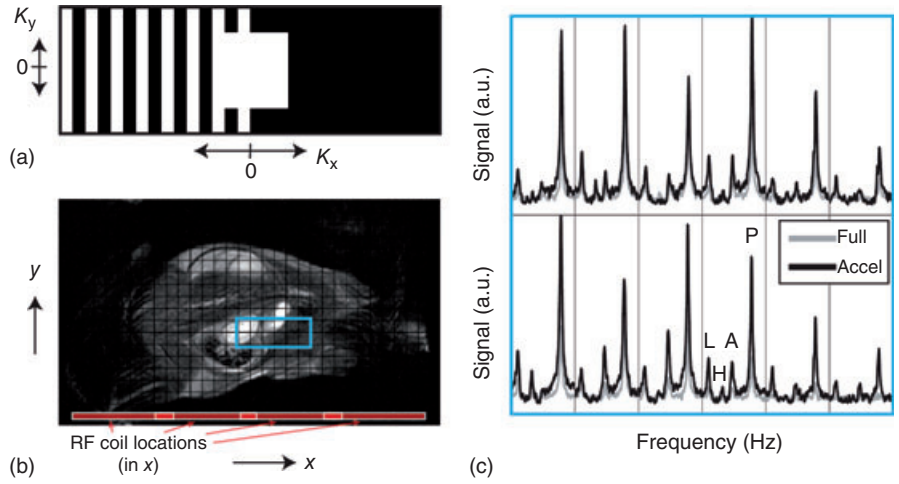

Figure 13. Example of parallel imaging MRSI results with HP [1-^{13}C]-pyruvate in a normal rat.[57] (a) The *k*-space undersampling pattern includes acceleration by skipping every other phase encode in k_x, a partial Fourier acquisition where half of *k*-space was not acquired, and a fully-sampled 6 × 6 center of *k*-space for an autocalibrated SENSE reconstruction. The overall acceleration factor is 2.9. This sampling pattern utilizes the multiple receive coils in the *x* direction (b), to reconstruct the image from undersampled data in k_x. (c) The accelerated spectra ('accel', acquired in 13.4 s) show improved structural depiction and SNR over the fully sampled spectra ('full', acquired in 39 s) due to reduced decay and conversion blurring during the scan time (P, pyruvate; L, lactate; A, alanine; H, pyruvate hydrate). (Reproduced with permission from Ref. 57. © John Wiley & Sons Ltd., 2013)

Table 1. Summary of HP MRS acquisition strategies

Acquisition strategy	Pros	Cons
Phase-encoded MRSI	Robust, flexible spectral content, large SBW, high spectral resolution	Slow, blurring during long acquisition times, RF inefficient
Rapid MRSI with switched gradients	Faster and more RF efficient than phase-encoded MRSI	Limited SBW and spatial resolution, trade-off with SNR efficiency
Model-based	Fast multiple metabolite imaging, faster and more RF efficient than rapid MRSI	Sensitive to choice of TEs, requires a priori knowledge of chemical shifts
Metabolite-specific imaging	Fastest strategy for imaging a single metabolite	Sensitivity to B_0 inhomogeneities, requires spectral separation of metabolites
SSFP	High SNR efficiency	Sensitivity to B_0 inhomogeneities, challenging to image multiple metabolites
2-D NMR	Direct measurements of spin-coupling and exchange, ultrafast methods available	Challenging to provide localized information
Compressed sensing	Accelerate acquisition based on HP MRS sparsity	Requires specialized acquisition and reconstruction strategy
Parallel imaging	Accelerate acquisition based on RF receive coil array	g-factor SNR penalty, requires tailored RF coil arrays

Summary of Acquisition Strategies

Table 1 shows a high-level summary of the HP MRS acquisition strategies discussed in this article, highlighting the major pros and cons of each strategy.

Summary

HP MRS has the ability to provide functional metabolic information in a rapid, noninvasive manner. However, the transient nature of the HP magnetization and the need for both spectral encoding and temporal resolution places unique demands on RF and acquisition strategies. This article has described current strategies for efficient HP MR that address these demands, as well as their limitations. From an MRS standpoint, HP agents exhibit some unique properties including the decay back to thermal equilibrium from the HP state, spin exchange, and metabolic conversion of the HP magnetization (see section titled 'Evolution of Hyperpolarized Agents'). Meanwhile, the rapid delivery of HP media from the polarizer to the subject represents a significant technical hurdle.

The primary consideration for RF pulse strategies (see section titled 'RF Pulse Strategies') is the irrecoverable effect that RF pulses have on the HP magnetization. VFA strategies aim to account for the effects of other RF pulses and can also address the effects of metabolic conversion. It is also very important to consider slice shifting due to chemical shift displacement artifacts and distortions in the slice profile resulting from repeated RF pulses in HP MR studies.

The choice of acquisition strategy (see section titled 'Acquisition Strategies') for HP MR is highly dependent on the application. MRSI methods provide excellent spectral coverage and resolution, but typically require relatively long scan times. Model-based and metabolite-specific imaging methods, on the other hand, can be very fast and efficient, but need to be tailored to the expected chemical shifts. Acceleration via compressed sensing and parallel imaging can be incorporated into most of these approaches to improve speed, which is crucial in most HP MR experiments.

Software Resources

Hyperpolarized MRI Toolbox (EPSI, variable flip angle schemes, model-based reconstruction code), https://github.com/agentmess/hyperpolarized-mri-toolbox.

Spectral-spatial RF pulse design package (MATLAB), https://github.com/agentmess/Spectral-Spatial-RF-Pulse-Design.

Gridding, http://mrsrl.stanford.edu/~brian/gridding/.

Nonuniform FFT (NUFFT), http://web.eecs.umich.edu/~fessler/code/.

Compressed Sensing, http://www.eecs.berkeley.edu/~mlustig/Software.html.

Acknowledgments

We thank the following people for their contributions to the figures in this article: Wenwen Jiang, Eugene Milshteyn, Michael Ohliger, Simon Hu, Angus Lau, and Charles Cunningham.

Biographical Sketches

Jeremy W. Gordon, PhD, is a postdoctoral scholar in the Department of Radiology and Biomedical Imaging at the University of California, San Francisco (UCSF). He has worked extensively on hyperpolarized ^{13}C MRI, focusing on novel acquisition and reconstruction methodologies, as well as imaging approaches for improved kinetic modeling. He has developed highly RF efficient, novel acquisition and reconstruction schemes to rapidly acquire hyperpolarized metabolic data.

Peder E.Z. Larson, PhD, is an Assistant Professor of Radiology and Biomedical Imaging at UCSF. He has worked extensively in the area of MRI pulse sequence design for clinical applications and developed numerous methods for hyperpolarized MR aimed at improving the efficiency and providing novel contrast. His pulse sequences were used in the first-in-man clinical trial of hyperpolarized ^{13}C-pyruvate in prostate cancer patients at UCSF.

Related Articles

Hyperpolarization Methods for MRS; CSI and SENSE CSI; High-Speed Spatial–Spectral Encoding with PEPSI and Spiral MRSI; Direct Water–Fat Imaging Methods: Chemical Shift-Selective and Chemical Shift-Encoded MRI; 2-D MR Spectroscopy Combined with 2-D/3-D Spatial Encoding; Integration of ^{13}C Isotopomer Methods and Hyperpolarization Provides a Comprehensive Picture of Metabolism; Hyperpolarized Carbon-13 MRI and MRS Studies

References

1. F. A. Gallagher, M. I. Kettunen, and K. M. Brindle, *Prog. Nucl. Magn. Reson. Spectrosc.*, 2009, **55**, 285.
2. L. Zhao, R. Mulkern, C.-H. Tseng, D. Williamson, S. Patz, R. Kraft, R. L. Walsworth, F. A. Jolesz, and M. S. Albert, *J. Magn. Reson. B*, 1996, **113**, 179.
3. K. R. Keshari and D. M. Wilson, *Chem. Soc. Rev.*, 2014, **43**, 1627.
4. N. Chattergoon, F. Martínez-Santiesteban, W. B. Handler, J. H. Ardenkjaer-Larsen, and T. J. Scholl, *Contrast Media Mol. Imaging*, 2013, **8**, 57.
5. A. P. Halestrap, *IUBMB Life*, 2012, **64**, 1.
6. S. J. Nelson, J. Kurhanewicz, D. B. Vigneron, P. E. Z. Larson, A. L. Harzstark, M. Ferrone, M. van Criekinge, J. W. Chang, R. Bok, I. Park, G. Reed, L. Carvajal, E. J. Small, P. Munster, V. K. Weinberg, J. H. Ardenkjaer-Larsen, A. P. Chen, R. E. Hurd, L.-I. Odegardstuen, F. J. Robb, J. Tropp, and J. A. Murray, *Sci. Transl. Med.*, 2013, **5**, 198ra108.
7. K. M. Brindle, *Prog. Nucl. Magn. Reson. Spectrosc.*, 1988, **20**, 257.
8. M. L. Zierhut, Y.-F. Yen, A. P. Chen, R. Bok, M. J. Albers, V. Zhang, J. Tropp, I. Park, D. B. Vigneron, J. Kurhanewicz, R. E. Hurd, and S. J. Nelson, *J. Magn. Reson.*, 2010, **202**, 85.
9. R. E. Hurd, Y.-F. Yen, J. Tropp, A. Pfefferbaum, D. M. Spielman, and D. Mayer, *J. Cereb. Blood Flow Metab.*, 2010, **30**, 1734.
10. S. M. Kazan, S. Reynolds, A. Kennerley, E. Wholey, J. E. Bluff, J. Berwick, V. J. Cunningham, M. N. Paley, and G. M. Tozer, Kinetic modeling of hyperpolarized 13C pyruvate metabolism in tumors using a measured arterial input function, *Magn. Reson. Med.*, 2013, **70**, 943.
11. K. Nagashima, *J. Magn. Reson.*, 2008, **190**, 183.
12. P. E. Z. Larson, A. B. Kerr, A. P. Chen, M. S. Lustig, M. L. Zierhut, S. Hu, C. H. Cunningham, J. M. Pauly, J. Kurhanewicz, and D. B. Vigneron, *J. Magn. Reson.*, 2008, **194**, 121.
13. Y. Xing, G. D. Reed, J. M. Pauly, A. B. Kerr, and P. E. Z. Larson, *J. Magn. Reson.*, 2013, **234**, 75.
14. R. F. Schulte, J. I. Sperl, E. Weidl, M. I. Menzel, M. A. Janich, O. Khegai, M. Durst, J. H. Ardenkjaer-Larsen, S. J. Glaser, A. Haase, M. Schwaiger, and F. Wiesinger, *Magn. Reson. Med.*, 2013, **69**, 1209.
15. N. Bahrami, C. L. Swisher, C. Von Morze, D. B. Vigneron, and P. E. Z. Larson, *Quant. Imaging Med. Surg.*, 2014, **4**, 24.
16. J. Pauly, P. L. Roux, D. Nishimura, and A. Macovski, *IEEE Trans. Med. Imaging*, 1991, **10**, 53.
17. C. Meyer, J. Pauly, A. Macovski, and D. Nishimura, *Magn. Reson. Med.*, 1990, **15**, 287.
18. A. Z. Lau, A. P. Chen, and C. H. Cunningham, *Magn. Reson. Med.*, 2012, **67**, 62.
19. R. F. Schulte, L. Sacolick, M. H. Deppe, M. A. Janich, M. Schwaiger, J. M. Wild, and F. Wiesinger, *NMR Biomed.*, 2011, **24**, 1068.
20. M. H. Deppe, K. Teh, J. Parra-Robles, K. J. Lee, and J. M. Wild, *J. Magn. Reson.*, 2010, **202**, 180.
21. A. B. Kerr and J. M. Pauly, Slice profile stabilization for segmented k-space magnetic resonance imaging. US Patent 5,499,629, 1996.
22. K. Golman, R. in't Zandt, and M. Thaning, *Proc. Natl. Acad. Sci. U. S. A.*, 2006, **103**, 11270.
23. M. J. Albers, R. Bok, A. P. Chen, C. H. Cunningham, M. L. Zierhut, V. Y. Zhang, S. J. Kohler, J. Tropp, R. E. Hurd, Y.-F. Yen, S. J. Nelson, D. B. Vigneron, and J. Kurhanewicz, *Cancer Res.*, 2008, **68**, 8607.
24. S. B. Reeder, J. H. Brittain, T. M. Grist, and Y.-F. Yen, *J. Magn. Reson. Imaging*, 2007, **26**, 1145.
25. F. Wiesinger, E. Weidl, M. I. Menzel, M. A. Janich, O. Khegai, S. J. Glaser, A. Haase, M. Schwaiger, and R. F. Schulte, *Magn. Reson. Med.*, 2012, **68**, 8.

26. J. W. Gordon, D. J. Niles, S. B. Fain, and K. M. Johnson, Joint spatial-spectral reconstruction and k-t spirals for accelerated 2d spatial/1d spectral imaging of 13c dynamics, *Magn. Reson. Med.*, 2013, **71**(4), 1435.
27. C. H. Cunningham, A. P. Chen, M. Lustig, B. A. Hargreaves, J. Lupo, D. Xu, J. Kurhanewicz, R. E. Hurd, J. M. Pauly, S. J. Nelson, and D. B. Vigneron, *J. Magn. Reson.*, 2008, **193**, 139.
28. A. Z. Lau, A. P. Chen, N. R. Ghugre, V. Ramanan, W. W. Lam, K. A. Connelly, G. A. Wright, and C. H. Cunningham, *Magn. Reson. Med.*, 2010, **64**, 1323.
29. W. Jiang, M. Lustig, and P. E. Z. Larson, Concentric rings k-space trajectory for hyperpolarized (13) c mr spectroscopic imaging, *Magn. Reson. Med.*, 2014, **75**(1), 19.
30. Y.-F. Yen, S. J. Kohler, A. P. Chen, J. Tropp, R. Bok, J. Wolber, M. J. Albers, K. A. Gram, M. L. Zierhut, I. Park, V. Zhang, S. Hu, S. J. Nelson, D. B. Vigneron, J. Kurhanewicz, H. A. A. M. Dirven, and R. E. Hurd, *Magn. Reson. Med.*, 2009, **62**, 1.
31. M. S. Ramirez, J. Lee, C. M. Walker, V. C. Sandulache, F. Hennel, S. Y. Lai, and J. A. Bankson, *Magn. Reson. Med.*, 2014, **72**, 986.
32. D. Mayer, Y. S. Levin, R. E. Hurd, G. H. Glover, and D. M. Spielman, Fast metabolic imaging of systems with sparse spectra: Application for hyperpolarized 13C imaging, *Magn. Reson. Med.*, 2006, **56**(4), 932.
33. M. Durst, U. Koellisch, A. Frank, G. Rancan, C. V. Gringeri, V. Karas, F. Wiesinger, M. I. Menzel, M. Schwaiger, A. Haase, and R. F. Schulte, *NMR Biomed.*, 2015, **28**, 715.
34. J. I. Jackson, C. H. Meyer, D. G. Nishimura, and A. Macovski, *IEEE Trans. Med. Imaging*, 1991, **10**, 473.
35. J. A. Fessler and B. P. Sutton, *IEEE Trans. Signal Process*, 2003, **51**, 560.
36. S. B. Reeder, A. R. Pineda, Z. Wen, A. Shimakawa, H. Yu, J. H. Brittain, G. E. Gold, C. H. Beaulieu, and N. J. Pelc, *Magn. Reson. Med.*, 2005, **54**, 636.
37. C. H. Cunningham, W. Dominguez Viqueira, R. E. Hurd, and A. P. Chen, *NMR Biomed.*, 2014, **27**, 212.
38. E. K. Brodsky, J. H. Holmes, H. Yu, and S. B. Reeder, *Magn. Reson. Med.*, 2008, **59**, 1151.
39. K. S. Nayak, C. M. Tsai, C. H. Meyer, and D. G. Nishimura, *Magn. Reson. Med.*, 2001, **45**, 521.
40. M. R. Smith, E. T. Peterson, J. W. Gordon, D. J. Niles, I. J. Rowland, K. N. Kurpad, and S. B. Fain, *IEEE Trans. Biomed. Eng.*, 2012, **59**, 45.
41. J. Svensson, S. Månsson, E. Johansson, J. S. Petersson, and L. E. Olsson, *Magn. Reson. Med.*, 2003, **50**, 256.
42. A. K. Grant, E. Vinogradov, X. Wang, R. E. Lenkinski, and D. C. Alsop, *Magn. Reson. Med.*, 2011, **66**, 746.
43. G. D. Reed, C. von Morze, R. Bok, B. L. Koelsch, M. Van Criekinge, K. J. Smith, H. Shang, P. E. Z. Larson, J. Kurhanewicz, and D. B. Vigneron, *IEEE Trans. Med. Imaging*, 2014, **33**, 362.
44. J. Leupold, S. Månsson, J. S. Petersson, J. Hennig, and O. Wieben, *MAGMA*, 2009, **22**, 251.
45. C. von Morze, S. Sukumar, G. D. Reed, P. E. Z. Larson, R. A. Bok, J. Kurhanewicz, and D. B. Vigneron, *Magn. Reson. Imaging*, 2013, **31**, 163.
46. G. Varma, X. Wang, and A. K. Grant, In *Proceedings of the ISMRM 22th Annual Meeting*, 2014, 3795.
47. H. Zeng, S. Bowen, and C. Hilty, *J. Magn. Reson.*, 2009, **199**, 159.
48. L. Frydman and D. Blazina, *Nat. Phys.*, 2007, **3**, 415.
49. M. Mishkovsky and L. Frydman, *ChemPhysChem*, 2008, **9**, 2340.
50. P. E. Z. Larson, A. B. Kerr, C. Leon Swisher, J. M. Pauly, and D. B. Vigneron, *J. Magn. Reson.*, 2012, **225C**, 71.
51. C. L. Swisher, P. E. Z. Larson, K. Kruttwig, A. B. Kerr, S. Hu, R. A. Bok, A. Goga, J. M. Pauly, S. J. Nelson, J. Kurhanewicz, and D. B. Vigneron, *Magn. Reson. Med.*, 2014, **71**, 1.
52. A. Arunachalam, D. Whitt, K. Fish, R. Giaquinto, J. Piel, R. Watkins, and I. Hancu, *NMR Biomed.*, 2009, **22**, 867.
53. M. Lustig, D. Donoho, and J. M. Pauly, *Magn. Reson. Med.*, 2007, **58**, 1182.
54. S. Hu, M. Lustig, A. Balakrishnan, P. E. Z. Larson, R. Bok, J. Kurhanewicz, S. J. Nelson, A. Goga, J. M. Pauly, and D. B. Vigneron, *Magn. Reson. Med.*, 2010, **63**, 312.
55. S. Hu, A. Balakrishnan, R. A. Bok, B. Anderton, P. E. Z. Larson, S. J. Nelson, J. Kurhanewicz, D. B. Vigneron, and A. Goga, *Cell Metab.*, 2011, **14**, 131.
56. M. A. Griswold, P. M. Jakob, R. M. Heidemann, M. Nittka, V. Jellus, J. Wang, B. Kiefer, and A. Haase, *Magn. Reson. Med.*, 2002, **47**, 1202.
57. M. A. Ohliger, P. E. Z. Larson, R. A. Bok, P. Shin, S. Hu, J. Tropp, F. Robb, L. Carvajal, S. J. Nelson, J. Kurhanewicz, and D. B. Vigneron, *J. Magn. Reson. Imaging*, 2013, **38**, 701.
58. P. J. Shin, P. E. Z. Larson, M. A. Ohliger, M. Elad, J. M. Pauly, D. B. Vigneron, and M. Lustig, *Magn. Reson. Med.*, 2014, **72**, 959.